

Strong Ground Motions From the 21 May 2021 M6.4 Yangbi Earthquake in Western China Obtained From a Dense Network of Accelerographs and Intensity Meters

Junju Xie (✉ xiejunju@163.com)

Institute of Geophysics China Earthquake Administration

Zhao An

Institute of Geophysics China Earthquake Administration

Lei Fu

Institute of Geophysics China Earthquake Administration

Kewei Li

Institute of Geophysics China Earthquake Administration

Xiaojun Li

Beijing University of Technology

Zengping Wen

Institute of Geophysics China Earthquake Administration

Jianwen Cui

Yunnan Earthquake Administration

Guoliang Lin

Yunnan Earthquake Administration

Pengfei Wang

University of California Los Angeles

Research Article

Keywords: 2021 Yangbi earthquake, Strong motion, Attenuation, Site effects, Directionality, Building code in China

Posted Date: October 19th, 2021

DOI: <https://doi.org/10.21203/rs.3.rs-977960/v1>

License:   This work is licensed under a Creative Commons Attribution 4.0 International License.

[Read Full License](#)

Abstract

The dense recordings of the 146 accelerometers in the near-source area clearly show the seismic wave propagation and spatial variability of strong ground motions during the 2021 Yangbi earthquake in Western China. The observation demonstrates that the near-source strong ground motions are characterized as short duration (< 15-20 s) but large ground accelerations and short-period spectral values. The dominant period of strong ground motions is generally short (0.1-0.5 s); whereas, in some records, the dominant period reaches 1.5 s while affected by soft and deep sediments. The observed peak ground velocities (PGVs) and long-period spectral accelerations (SAs) over 1.0 s are relatively weak and attenuate rapidly with distance, resulting in a small damage zone of earthquake intensity VIII. We find many anomalies in the distribution of ground motion intensity measures (IMs) caused by local topography and soft sediments. Topographic amplification mainly affects PGAs and short-period SAs below 1.0 s, while the soft sediments show strong amplification effects in the long-period SAs over 1.0 s. The Next-Generation Attenuation (NGA) -West2 models have a good estimation of peak ground accelerations (PGAs) and short-period SAs, but tend to over-predict long-period SAs over 1.0 s for this event. Strong directionality is observed in the near-fault, where observed PGAs, PGVs and SAs in the fault parallel (FP) component are much larger than those in the fault normal (FN) component; which is validated by the clear evidence of different building damage patterns along the FN and FP directions. Response spectra of near-fault ground motions are higher than the code design spectra in China at periods of around 0.1 s, but lower than the code at periods over 0.5 s. This result can explain why the building structures (with fundamental periods of 0.5 s or higher) constructed following the building code show relatively rare damage in the near-fault region.

1 Introduction

On 21 May 2021, at 13:48 UTC (21:48 Beijing time), a M 6.4 earthquake took place in Yangbi county in Western China, about 280 km from Kunming, the capital city of Yunnan province. According to the report of China Earthquake Networks Center (CENC, <https://www.cenc.ac.cn/>), the epicenter is located at N25.67°, E99.87° near the Xiuling village, southwest of Yangbi county. Ground shaking of this earthquake can be felt in Puer, Panzihua and Kunming city. The most violent shaking was in Yangbi county, causing casualties and the collapse of many mud-wood structures. Severe shaking results in the damage of various cultural relics and historic buildings in the Dali ancient city zone. The maximum intensity is VIII in the Chinese seismic intensity scale. The intensity scale is divided into 12 levels from I to XII according to the degree of people's feeling, the response of utensils, and damage of buildings, etc. (SAMG, 2020). The most seriously damaged zone covers an area of about 170 square kilometers, including three townships, Cangshan West Town, Yangjiang town, and Taiping Township (CEA 2021). The area with earthquake intensity over VI is more than 6000 square kilometers, involving 6 counties and cities of Dali Prefecture.

Yangbi county is located in the Red River fault zone and belongs to an earthquake-prone area. The largest recorded earthquake in this area in history was the Dali M 7 earthquake on March 16, 1925. The sequence of the 2021 Yangbi earthquake includes the M 6.4 mainshock, the largest foreshock of M 5.6 occurring 27

minutes before the mainshock, and the largest aftershocks of M 5.0 and M 5.2 about 1 hour after the mainshock. The relocation results of Yangbi earthquake sequences show that aftershocks are distributed in the North-West direction. The seismogenic fault is inclined to the southwest with a fracture length of about 20km, and aftershocks are mainly concentrated in the depth of 6-17 km (Yang et al. 2021). Inverse analysis of the rupture process suggested that seismic energy of the mainshock is mainly released in the first 8 seconds. The mainshock is dominated by a strike-slip fracture mechanism, of which the seismic moment magnitude is Mw 6.1. The extreme sliding area locates in the southeast of the epicenter, and the main fracture length is about 12-15 km (Zhang et al. 2021).

The M 6.4 Yangbi mainshock was well-recorded by the dense network of accelerometers located in Yunnan province. This paper introduces an overview of strong motion observations by strong motion stations and intensity stations near the source. In addition, three-component recordings from 146 stations within 160 km from the earthquake epicenter are selected to investigate characteristics of strong ground motion from the M 6.4 Yangbi earthquake. We present the analysis results on the spatial variability and attenuation of observed ground motion intensity measures (IMs) with distance. Local site effects and directionality of near-fault ground motion are revealed based on our study.

2 Strong Motion Observation

There are 1857 strong motion observation stations all over Yunnan province; 611 stations use accelerographs, while 1246 stations are equipped with intensity meters. Over 170 accelerographs and intensity meters were triggered during the mainshock. These stations are distributed in Yunnan province with epicentral distances from 8.1 km to 300 km. Figure 1 shows the distribution of triggered accelerographs and intensity meters within 160 km from the epicenter, including 9 strong motion stations and 137 intensity stations. The strong motion stations belong to the National Strong Motion Observation Network System (NSMONS) of China (Li et al. 2008). These stations are equipped with Kinematics instruments of ETNA/K2 model with full-scale set of $2g$ and sample rate of 200 samples/sec. The high dense intensity stations are deployed as a part of the National System for Seismic Intensity Rapid Reporting and Earthquake Early Warning in China (CEA 2019). The intensity stations use low-cost P-Alert accelerometers with MEMS sensors. The signal resolution of a MEMS P-Alert accelerometer is 16 bits with a full scale of $\pm 2g$, and the sampling rate is 100 samples/sec. The intensity stations are used to fill in the gaps between higher-quality sensors and provide valuable observations for earthquake early warning to reduce the detection time for a damaging earthquake.

Although the self-noise level of intensity stations (about 0.1 cm/s^2) is higher than strong motion stations, we find that the recordings by intensity stations are in high consistency with nearby strong motion stations after comparison. Figure 2 compares three-component acceleration and velocity time series obtained from intensity station L0101 and nearby strong motion station 53DLY. Response spectra and horizontal-to-vertical spectral ratio (HVSr) with respect to periods are presented in the same figure. The comparison shows that the observed wave trains and patterns in the acceleration and velocity time series of these two stations are highly consistent. Meanwhile, the HVSr curves of both 53DLY and L0101

records demonstrate clear amplification at periods of 1.5-2.5 s in the horizontal components due to local site effects. Since 53DLY station is closer to Erhai Lake with deep sediments, the PGAs, PGVs, and spectral values at long-period over 1.0 s recorded at 53DLY are a little larger than L0101. However, the acceleration and velocity waveforms and response spectra of these two recordings are comparable on the whole. The good performance of MEMS accelerometers in providing reliable waveforms, PGA, PGV, and response spectra below 10.0 s (<0.1 Hz) has been validated by many previous studies (Cochran et al. 2011; Jyh et al. 2017). These findings suggest that data of MEMS accelerometers is well qualified to explore spatial variability in ground motions and for further studies of engineering purposes.

Besides the free-field stations equipped with accelerographs and intensity meters, two structure arrays located in Dali Economic Development Zone and Longjiang Bridge are triggered in the mainshock. The structure array in Dali Economic Development Zone has a 10-point strong motion observation system deployed by Yunnan Earthquake Administration. The array is about 41.5 km from the epicenter. The smallest horizontal PGAs are observed in the basement with peaks of 34.1 cm/s^2 , 32.5 cm/s^2 ; the largest PGAs are observed on the 26th floor with peaks of 82.7 cm/s^2 , 92.2 cm/s^2 . Longjiang Bridge is 150 km from the epicenter. The authors of this paper in the Institute of Geophysics, China Earthquake Administration (CEA), Beijing University of Technology, and Yunnan Earthquake Administration participated in the post-earthquake reconnaissance missions. We collected 11 recordings from the 12-point strong motion observation system of the Longjiang Bridge structure array; one of the 12 points did not obtain records due to a GPS timing problem. As a part of the post-earthquake reconnaissance mission, we build a temporary topographic array of 5 observation points around Yangbi county town (see Fig. 9). Station 179 and 172 are located in Xiuling village on the hill close to the epicenter, one station of No. 175 on the hillside from Yangbi county town to Xiuling village, one station of No. 173 at the foot of the hill, one station of No. 177 in the Huaian village in the small basin of Yangbi county town. Over 40 aftershocks were captured by the temporary array, with the largest magnitude of 4.1. The maximum PGA is 65 cm/s^2 recorded by station 179 from the M 4.1 aftershock.

3 Spatial Distribution Of Strong Ground Motion During The Mainshock

In the Yangbi M6.4 mainshock, the near-field strong motion records showed an obvious baseline offset. We noted that the traditional filtering method often filters out the useful displacement information and causes phase distortion in the velocity waveforms (Xie 2019). Here we processed the large amplitude near-field recordings using a multi-consecutive-segment baseline correction method (Boore 2001; Xie et al. 2014). For far-field recordings without permanent displacement, a Butterworth filter with a 0.05–50 Hz bandwidth was applied. Records with low signal-to-noise ratio or abnormal acceleration waveforms were removed in this study.

We examined the spatial variation of waveform patterns and attenuation of ground motion amplitudes with distance. Figure 3 shows the observed North-South (NS) component waveforms sorted by distance from the epicenter along the A-A' profile (see Fig. 1). The top and bottom panel shows the waveforms along the directions of epicenter to A' and to A, respectively. Overall, the duration of near-source strong

shaking is very short, less than about 15 s. The record of 51YBX station has the latest arrival of waveform and the largest PGA of 720.3 cm/s^2 and PGV of 29.9 cm/s . The waveforms clearly depict wave propagation from the earthquake source to the observation sites and attenuation in ground motion amplitude with increasing epicentral distance. However, we notice an exception of station 53BCJ, of which both PGA and PGV are much larger than the closer station 53BTH. We compared the horizontal NS and EW component acceleration and velocity waveforms, response spectra, and computed HVSR curves of the record 53BCJ with 53BTH. The two recording stations are in the same azimuth relative to the source and have a comparable distance of about 70 km from the epicenter. However, the 53BTH station locates on a limestone rock site in the back hill near Caifeng village in Binchuan county, while the 53BCJ station locates in the small Binchuan basin with alluvial sediments. Figure 4 shows that the PGAs and PGVs of 53BCJ record are approximately 3-4 times of those of 53BTH. The response spectra of 53BCJ are much higher than those of 53BTH. The HVSR curves indicate that ground motions of the 53BCJ record are strongly amplified due to soft alluvial sediments at the local site, especially at periods of 2-4 s.

Figure 5 shows an overview of the spatial variability of observed horizontal PGA, PGV and SAs at periods $T=0.2 \text{ s}$, 0.5 s , 1.0 s , and 3.0 s . The horizontal ground motion parameter is presented as the geometric mean of the EW and NS components. The largest PGA and PGV are recorded at station 51YBX, which is close to the epicenter. All 6 recordings with PGA over 100 cm/s^2 and PGV over 10 cm/s are located within the isoseismic circle of intensity VI, less than 30 km from the source. We find a sharp decrease of observed spectral values with increasing periods. The largest SA value is 725.0 cm/s^2 at $T=0.2 \text{ s}$, while only 38.8 cm/s^2 at the period of $T=3.0 \text{ s}$. At period $T=1.0 \text{ s}$, only three records of 53YBX, L0103, and L2701 have SAs larger than 100 cm/s^2 . At period $T=3.0 \text{ s}$, there are only two records with SAs larger than 20 cm/s^2 , obtained by the 53YBX and 53DLY stations. In the distribution of PGA (Fig. 5a) and short-period SA at $T=0.5$ (Fig. 5d), we note many recordings with much larger IMs than the nearby stations, especially at far distance of 100-160 km. They are mainly caused by local topographic amplification effects. We will further investigate these anomalies in the latter section.

The seismic intensity distribution shows that the serious damage zone is relatively small and concentrated within the earthquake intensity VIII circle. Compared with PGA and short period SAs, the spatial variability of PGV and long period SAs at 1.0 s and 3.0 s correlates much better with the damage distribution. We note an outlier of station 53SDX located 125.8 km southwest from the epicenter, with recorded PGV and long-period SAs of 1.0 and 3.0 s much larger than nearby stations. The 53SDX station locates in the center of the small Shidian basin. The borehole log shows the site is covered with soft sediments of peats and clay over 40 m. Response spectra and HVSR curves of the 53SDX record in Fig. 6 show strong amplification in horizontal ground motions relative to the vertical component, especially at periods of 1.0 - 3.0 s . Meanwhile, the dominant period of horizontal response spectra of 53SDX reaches about 1.5 s , which is much longer than the nearby sites.

In the high-rise buildings in the main urban area (Xiaguan Town) of Dali City, about 34 kilometers away from the epicenter, people felt strong shaking, and the auxiliary components such as infilled walls were

damaged to varying degrees. Our analysis for station 51DLY in Fig. 2 shows that ground motions near Erhai Lake are strongly amplified at periods between 1.5 to 3.0 s due to soft sediments of local sites. We consider the strong low-frequency shaking between 1.5 to 3.0 s as an important factor causing damage in high-rise buildings in Dali City far away from the epicenter.

4 Attenuation In Intensity Measures And Comparison With NGA-west2 Models

Inversion results of the rupture process showed that the ruptured area was relatively small, with a main fracture length of about 12-15 km, and the main ruptured area is close to the epicenter (Zhang et al. 2021). Here we use the epicentral distance to estimate the attenuation of strong motion with distance. Figure 7 demonstrates the variation of observed horizontal PGA, PGV, and SAs with epicentral distance. We compare the attenuation of PGA, PGV, and SAs with distance observed during this event with the NGA-West2 models (Bozorgnia et al. 2014). The vast majority of the observation stations are located on class II sites (based on the Chinese site class, Li et al. 2008; MHURC 2010), which falls in the NEHRP site class between C and D (BSSC 2020). Hence, we choose a representative value of $V_{s30}=360\text{m/s}$ in the NGA - West2 models for comparison. The comparison shows that the average level (mean fit) of observed PGA and short period SA at 0.2 s during this event is close to the median predictions of NGA-West2 models. However, at periods over 0.5 s, the average level of observed SA is generally lower than the NGA-West2 models. The results show that NGA-West2 models accurately estimate PGA and short period SA, but over-predict long-period SA over 1.0 s for this event. Similar comparison results have been shown during the 2008 Wenchuan and 2013 Lushan earthquake occurred in Western China (Wen et al. 2010; Xie et al. 2014), which indicates the NGA-West2 models showing a systematic bias of over-predicting long-period SA for Western China.

Figure 7 also shows the clear bias of observed PGAs, PGVs, and SAs of individual sites relative to the mean curve of this event. Within the distance of 20-50 km, observed IMs at stations 53DLY, L0101, L2701, and L2703 are much higher than the mean curve, especially for PGV and long-period SA over 1.0 s. By site investigation, we find that these 4 stations locate near either Erhai Lake or small basins with relatively soft and deep sediments. The observation indicates strong amplification in IMs due to soft and deep sediments. Within the distance of 110-150 km, as shown in Fig. 5d, observed SA values of 0.5 s at stations 53SDX, E0101, E2404, L2602, M8113, Q0105, and Q2302 (colored in blue and red) are much higher than the mean curve of this event. Interestingly, we find two kinds of site effects from the observation of these 7 sites. The M8113, Q0105 and Q2302 records (red triangles) have PGAs and short-period SAs higher than the mean curves, but at the period over 1.0 s, the observed SAs tend to close to or even much lower than the mean. By site investigation, we found these intensity stations are co-located in communication base stations deployed on hills in order to get good signals. The discrepancy shown in M8113, Q0105 and Q2302 records reveals a kind of site effects due to topography. On the other hand, the 53SDX, E0101, E2404 and L2602 records (blue triangles) generally having all IMs higher than the mean curves shows the evidence of strong amplification due to soft and deep sediments.

To show the difference between the site effects caused by the topography and soft sediment, Fig. 6 compares the three-component acceleration and velocity time series, 5% damping response spectra and HVSR curves of typical recordings obtained in station Q0105 with 53SDX. Different from the soft site condition of 53SDX, station Q0105 is deployed on mountainside and with relatively shallow sediment. The comparison shows the Q0105 record has more high frequency content in the acceleration and velocity waveforms than that of 53SDX. Although the PGAs of record Q0105 are slightly larger than 53SDX, the PGVs are obviously smaller than 53SDX (Fig. 6a, b). The response spectra show that dominant periods of Q0105 and 53SDX record are about 0.5 and 1.5 s, respectively (Fig. 6c). Furthermore, the HVSR curves indicate that the horizontal components of Q0105 are amplified at periods of about 0.5 s, while those of 53SDX are strongly aggravated at periods of 1-2 s. Both with epicentral distances of 120-130 km, these two recordings have similar path attenuation effects. Meanwhile, the near-source effects can be ignored in such far distance relative to a M 6.4 source. Thus, the obvious discrepancy in waveforms and frequency content between these two recordings can be mainly attributed to the differences of local site condition. Clear difference of these two recordings reveal the different impact pattern of local topography and soft sediments.

5 Effects Of Ground Shaking

5.1 Near-fault strong motion directionality and caused damage pattern

Two recordings are observed close to the epicenter with a distance of fewer than 10 km. We investigate near-fault strong motion directionality by comparing the observation in the fault parallel (FP) and fault normal (FN) direction. Figure 8a-b show the FP and FN components of acceleration (Fig. 8a) and velocity (Fig. 8b) time series and response spectra for 5% damping ratio at these two stations of 53YBX and L2203 which are located in the intensity VIII and VII zone respectively in Yangbi county (see Fig. 1). The fault parallel PGV of the 53YBX record is over 2 times larger than the fault normal, and the fault parallel PGA and response spectra at periods over 0.4 s are much higher than the fault normal. The L2203 record observed in the intensity VII zone also shows an apparent discrepancy between the FP and FN components, with higher PGA and PGV in the FP direction. The comparison of ground motions observed in the FP and FN direction demonstrates strong directionality in the near-fault during this event. Meanwhile, the acceleration response trace shown in Fig. 8c-f indicate a clear predominant direction along the FP for near-fault ground motion in Yangbi county town, especially at periods of 0.5, 1.0 and 3.0 s.

From June 6 to 10, 2021, a joint scientific research team of the Institute of Geophysics, CEA, Beijing University of technology, and Yunnan Earthquake Administration conducted an earthquake damage survey on the most severely damaged Yangbi county and surrounding villages, as well as the ancient city and urban area of Dali. It mainly investigates the types of housing structures, including brick concrete structure, frame structure, earth-wooden structure, and other rural dwellings. Figure 9 shows the location

of seismic damage investigation sites and deployed topographic array in the most severely damaged Yangbi county. Figure 10a-b show two teaching buildings (RCF structure) in a primary school of Xiajie village in Yangbi county town. The teaching building along the FN direction is basically intact and able to be used normally. In contrast, the other one along the FP direction is damaged with obvious cracks and wall spalling and is suspended for use. Figure 10c shows a comparison of two earth-wooden houses in Huaian village north of Yangbi county town. The tiles of the houses facing FN direction are relatively intact, and the houses facing FP direction are seriously damaged with shuttle tiles and walls. The strong directionality of near-fault ground motion was observed in this earthquake; that is, ground motion in FP direction is greater than that in FN direction. This phenomenon can explain the typical seismic damage differences in the FN and FP direction and might be related to the rupture direction of the seismogenic fault. We also compared the two horizontal response spectra of stations 53YBX and L2203 observed during the aftershocks. We find no clear directionality in the near-fault ground motion; that is, ground motion amplitudes are very close between the two horizontal components. We consider that the strong directionality observed in the mainshock can not be caused by the local site effect, while it should be related to the focal mechanism of the mainshock.

5.2 Comparison of near-fault response spectra with building code in China and observations of structure damage

Figure 11 illustrates the comparison of observed near-fault response spectra (5% damping) with code design spectra in China. The dominant periods of horizontal response spectra of record 53YBX and L2203 are small and about 0.1 s and 0.2 s, respectively. In the intensity VIII zone, the FP and FN component spectra of the 53YBX record are even higher than the code design spectra for the intensity IX zone at period around 0.1 s. However, at periods of 0.5-3.0 s close to the fundamental period of building structures, both the FP and FN components are lower than the code design spectra for the intensity VIII zone. In the earthquake intensity VII zone, the L2203 record has spectra values larger than the code design spectra for intensity VII zone at period around 0.3 s. Still, at periods over 0.5 s, the spectra are much lower than the code spectra.

Figure 12 shows the typical earthquake damage phenomena in (a-e) Xiajie village and (f-g) Laojie of Yangbi county town and (h-i) Huaian village, such as collapse and shear failure of filled wall of earth-wooden structures (Fig. 12a-b), overall deviation of the brick-concrete house caused by foundation failure (Fig. 12e-f), shear failure of brick concrete courtyard wall (Fig. 12h). Among them, Fig. 12c-e shows the overall offset of a brick concrete house (left side) in Xiajie village, colliding with adjacent houses due to foundation failure. A distance of 50 cm was reserved between the two buildings, but they touched each other after the earthquake. The earthquake also caused the building on the left to rotate. This damage may result from the shallow foundation and slope in the foundation of building, and the asynchronous displacement occurred in the earthquake.

We find that most of the gables of local earth-wooden houses are rammed walls, which are seriously damaged in this earthquake. The damage includes peeling and cracking of gables, cracking at the

junction of vertical and horizontal walls, flash collapse of some gables (Fig. 12a-b, i). The wooden structures of civil buildings are basically intact, but some wooden columns are damaged due to the decline of bearing capacity (Fig. 12g). The seismic damage of frame and brick concrete buildings is relatively light, and the main damage is tile falling, wall peeling and infilled wall cracks. The brick concrete structure with ring beam and structural column structure generally has good seismic performance with less damage and fewer cracks on the wall.

Figure 13 shows the typical earthquake damage in Xiuling village near the epicenter. Xiuling village is located about 15 km northwest of Yangbi county town. The survey indicates that the Xiuling village suffers the hardest during this earthquake. Figure 13a-b show the overall collapse of the adobe wall of two earth-wooden houses, with residual wooden load-bearing pillars, which are basically intact. The wall thickness reaches 50-60cm, made of local cohesive soil and water without adding traditional cohesive media such as rice straw or glutinous rice. The adobe wall itself has a large self-weight and lacks shear capacity. In addition, the wall is located outside the column and lacks a restraint connection with the column, so it is easy to collapse in an earthquake. Figure 13c shows the damage of a brick-concrete building of Xiuling village neighborhood committee. The aged wooden frame on the roof of the building collapsed and a large number of tiles fell, but the wooden load-bearing pillars were basically intact without fracture and collapse. Figure 13d reflects the impact of the strong polarity of near-fault ground motion in Xiuling village. The tiles of the front house along the FN direction are relatively intact, but serious shuttle tiles appear in the rear houses along the FP direction. In general, the earthquake damage in Xiuling village is more serious than that in Yangbi county town. Xiuling village is located on the ridge near the top of the mountain, and the mountain inclination is about 30°, resulting in an obvious topographic amplification effect.

According to the earthquake damage investigation in Yangbi county and its surrounding areas, the newly-built brick concrete and frame structures constructed following the building code have good performance. In contrast, old brick concrete structures with a serious decline in bearing capacity and earth-wood houses without following the regulation are seriously damaged. Characteristics of observed near-fault response spectra can explain the damage pattern observed in the near-fault for different building structures.

Summary

The 21 May 2021 Yangbi M 6.4 earthquake was well recorded by a dense network of strong motion stations and intensity stations in China. The observation shows that the spatial variability of near-source strong ground motions is strongly affected by the earthquake source and local site effects. The recordings clearly demonstrate the characteristics of short duration (< 15-20 s) and small (0.1-0.5 s) dominant period of strong ground motion in the near-source. Observed PGVs and long period SAs over 1.0 s are relatively weak and attenuate rapidly with distance, showing a good coincidence with the damage spatial variation pattern.

The anomalies in the distribution of near-source strong ground motions are mainly caused by local site effects due to topography and soft sediments. Local topography mainly affects PGA and short-period response spectrum values below 1.0 s, which are observed by intensity stations co-located in communication base stations. The reason for strong topography effects is that these communication base stations are deployed on hills to get good signals. Meanwhile, the soft covering soil has strong amplification effects in the long-period response spectrum values over 1.0 s. The attenuation of ground motion IMs also reveals two kinds of different local site effects.

Near-fault ground motion shows strong directionality with a clear predominant direction, leading to different building damage patterns along the FN and FP directions. The observed near-fault motions at short period around 0.1 s can be higher than the code design spectra in China, but they are much lower than the design spectra at periods close to the fundamental periods of building structures. Characteristics of near-fault strong motion provide a good explanation for the damage phenomenon observed in Yangbi county town. The earth-wooden houses are seriously damaged, with rammed earth gable and outer longitudinal wall totally collapsed, and it is difficult to repair after the earthquake. However, the newly-build fortification buildings of brick-concrete and frame structures performed well in the earthquake. We consider improving the seismic fortification of engineering structures to be the most effective means to reduce earthquake disasters.

Data and Resources

The strong motion dataset consists of data provided by China Earthquake Networks Center (CENC), available by application through the website of National Earthquake Data Center (<http://data.earthquake.cn>) (last accessed on 20 August 2021). The geophysical maps produced in this study are produced using Generic Mapping Tools (GMT; Wessel and Smith, 1991).

Declarations

Competing Interests:

The authors acknowledge that there are no conflicts of interest recorded.

Acknowledgements

The author acknowledges the China Earthquake Networks Center (CENC) for providing strong motion data. The data are available by application through the website of National Earthquake Data Center (<http://data.earthquake.cn>). Financial support of this study was fully provided by the National Key Research and Development Program of China (Grant Number 2018YFE0109800), the Special Fund of Institute of Geophysics, China Earthquake Administration (DQJB16A02, DQJB21Y42), and Natural Science Foundation of China (51738001). We thank Chenghao Lv for the helpful comments of improving the manuscript.

References

1. Abrahamson NA, Silva WJ, Kamai R (2014) Summary of the ASK14 ground motion relation for active crustal regions. *Earthquake Spectra* 30:1025–1055
2. Boore DM (2001) Effect of baseline corrections on displacement and response spectra for several recordings of the 1999 Chi-Chi, Taiwan, earthquake. *Bull Seism Soc Am* 91:1199–1211
3. Boore DM, Stewart JP, Seyhan E (2014) NGA-West2 equations for predicting PGA, PGV, and 5% damped PSA for shallow crustal earthquakes. *Earthquake Spectra* 30:1057–1085
4. Bozorgnia Y, Abrahamson NA, AlAtik L, Ancheta TD, Atkinson GM, Baker JW, Baltay A, Boore DM, Campbell KW, Chiou BSJ (2014) NGA-West2 Research Project. *Earthquake Spectra* 30:973–987
5. Building Seismic Safety Council (BSSC) (2020) NEHRP Recommended Seismic Provisions for New Buildings and Other Structures. Building Seismic Safety Council, Federal Emergency Management Agency, Washington D.C.
6. Campbell KW, Bozorgnia Y (2014) NGA-West2 ground motion model for the average horizontal components of PGA, PGV, and 5% damped linear acceleration response spectra. *Earthquake Spectra* 30:1087–1115
7. China Earthquake Administration (CEA) (2019) Scientific Design of China Earthquake Science Experimental Field. China Standard Press, Beijing (in Chinese)
8. China Earthquake Administration (CEA) (2021) Intensity map of 5·21 Yangbi M6.4 earthquake in Yunnan province. http://www.yndzj.gov.cn/yndzj/_300559/_300651/629959/index.html (in Chinese)
9. Chiou BSJ, Youngs RR (2014) Update of the Chiou and Youngs NGA model for the average horizontal component of peak ground motion and response spectra. *Earthquake Spectra* 30:1117–1153
10. Cochran ES, Lawrence JF, Kaiser A, Fry B, Chung A, Christensen C (2011) Comparison between low-cost and traditional MEMS accelerometers: a case study from the M7.1 Darfield, New Zealand, aftershock deployment. *Ann Geophys* 54:728–737
11. Li X, Zhou Z, Yu H, Wen R, Lu D, Huang M, Cui J (2008) Strong motion observations and recordings from the great Wenchuan Earthquake. *Earthq Eng Eng Vib* 7:235–246
12. Ministry of Housing and Urban-Rural Construction of the People's Republic of China (MHURC) (2010) Code for Seismic Design for Buildings (GB 50011-2010). China Building Industry Press, Beijing (in Chinese)
13. Jyh J, Chao WA, Wu YM, Chen CC, Lin CH (2017) How well can we extract the permanent displacement from low-cost MEMS accelerometers? *Sensors* 17:2643
14. State Administration of Market Regulation (SAMR) (2020) The Chinese seismic intensity scale (GB17742-2020). China Standards and Quality Inspection Press, Beijing (in Chinese)
15. Wen Z, Xie J, Gao M, Hu Y, Chau KT (2010) Near-Source Ground Motion Characteristics of the Ms8.0 Wenchuan Earthquake. *Bull Seism Soc Am* 100:2425–2439
16. Xie J (2019) Strong-Motion Directionality and Evidence of Rupture Directivity Effects during the Chi-Chi Mw 7.6 Earthquake. *Bull Seism Soc Am* 109:2367–2383

17. Xie J, Li X, Wen Z, Wu C (2014) Near-Source Vertical and Horizontal Strong Ground Motion from the 20 April 2013 Mw 6.8 Lushan Earthquake in China. *Seismol Res Lett* 85:23–33
18. Yang T, Zhong Y, Fang L (2021) Aftershocks relocations of Yangbi M_s 6.4 earthquake. <http://www.chinarraydmc.cn/highlights/queryPage> (in Chinese)
19. Zhang X, Zhang Y, Xu L, Chen Y (2021) Rupture process of the Yangbi M_s 6.4 earthquake. <http://www.cea-igp.ac.cn/kydt/278248.html> (in Chinese)

Figures



Figure 1

Distribution of strong motion stations and intensity stations selected in this study. Strong motion stations and intensity stations are shown in rectangles and triangles respectively. The red shaded areas denote the intensity distribution based on seismic damage investigation (CEA, 2021). The elliptical shaded areas from inside to outside are characterized by Chinese earthquake intensity VIII, VII and VI, respectively.

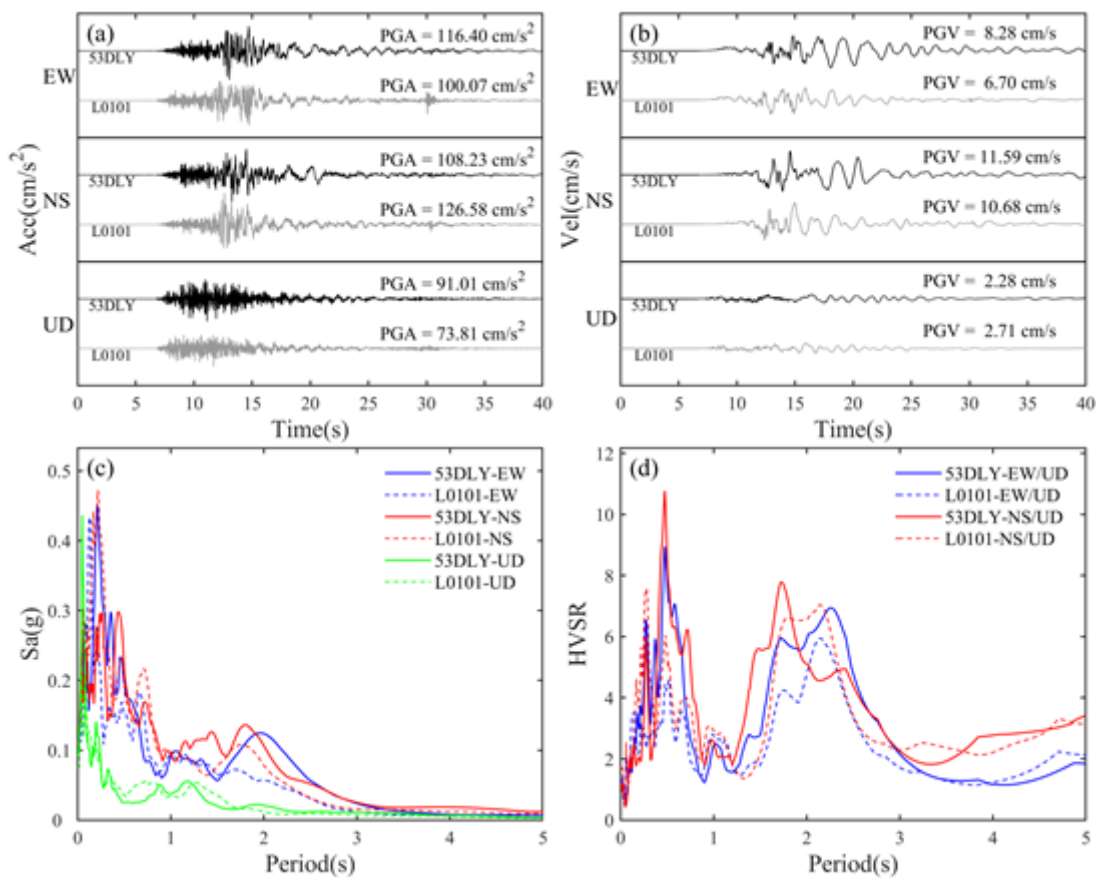


Figure 2

North-South (NS), East-West (EW) and vertical (UD) component (a) acceleration and (b) velocity time series, (c) response spectra and (d) HVSR curves recorded at strong motion station 53DLY and intensity

station L0101. Note that two stations are close to each other (see Fig. 1)

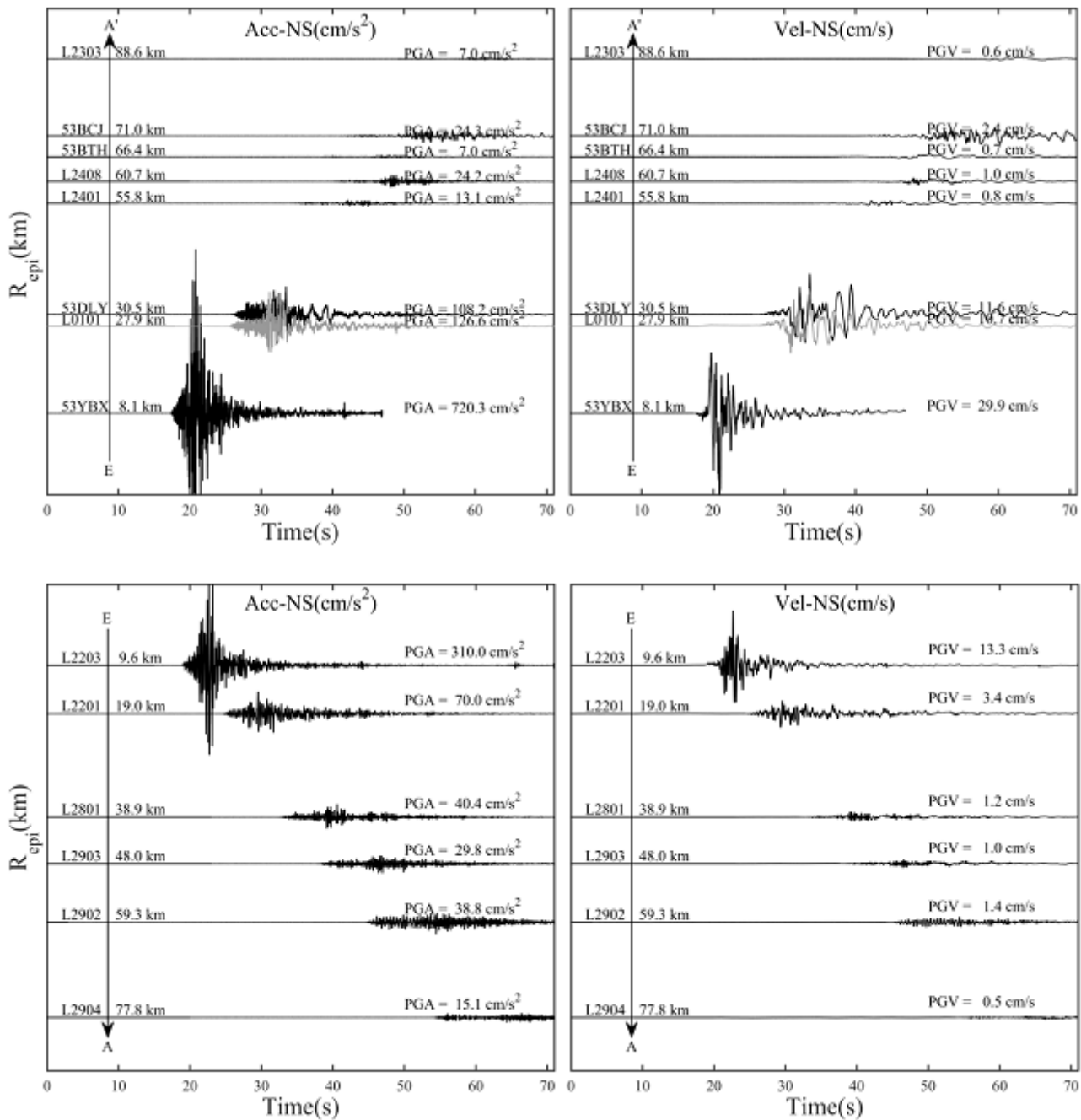


Figure 3

Comparison of observed acceleration and velocity waveforms of North-South (NS) components sorted by epicentral distance along the A-A' direction (see Fig. 1 on their exact locations). Acceleration velocity waveforms are plotted versus the station's distance from the epicenter and all time axes are plotted with respect to a fixed time frame.

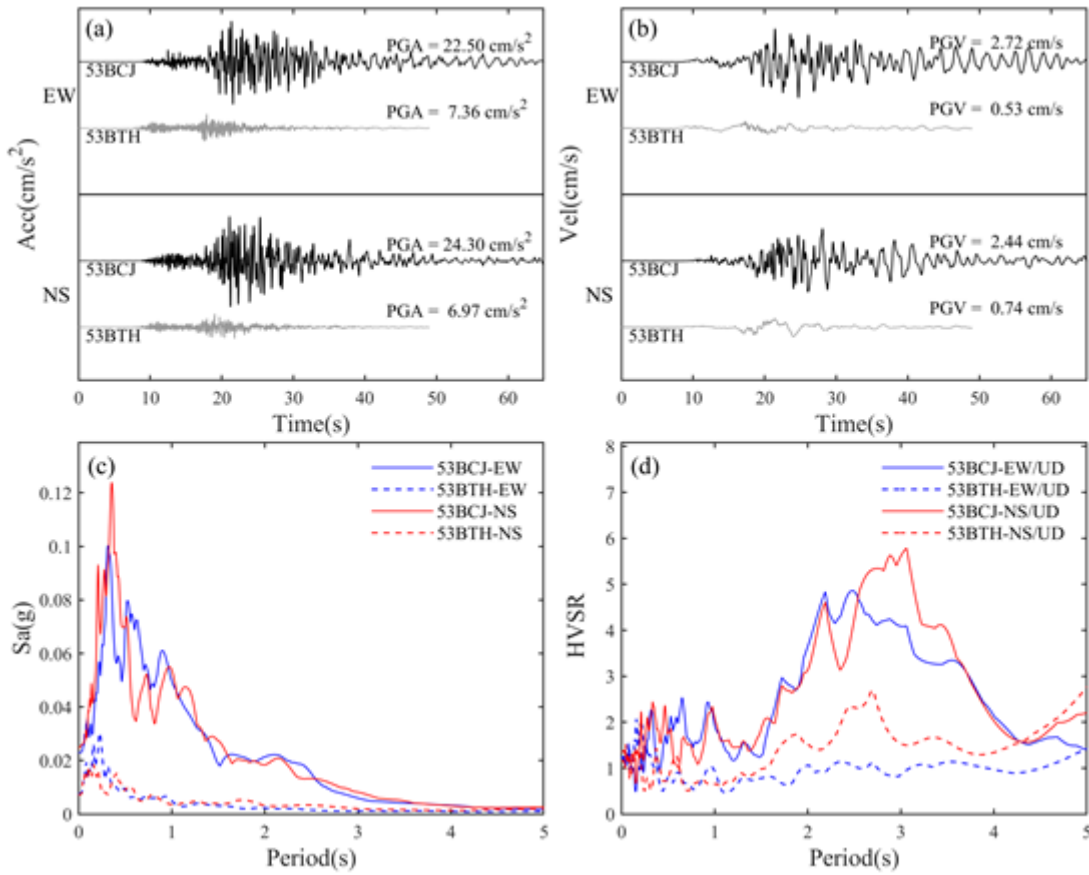


Figure 4

Spatial distribution of observed horizontal (a) PGA, (b) PGV, and SAs at period $T =$ (c) 0.2 s, (d) 0.5 s, (e) 1.0 s and (f) 3.0 s. Strong motion stations and intensity stations are shown in rectangles and triangles respectively. The color shaded elliptical areas indicate the intensity map given by CEA (2021). The elliptical areas from inside to outside are characterized by Chinese earthquake intensity VIII, VII and VI, respectively.

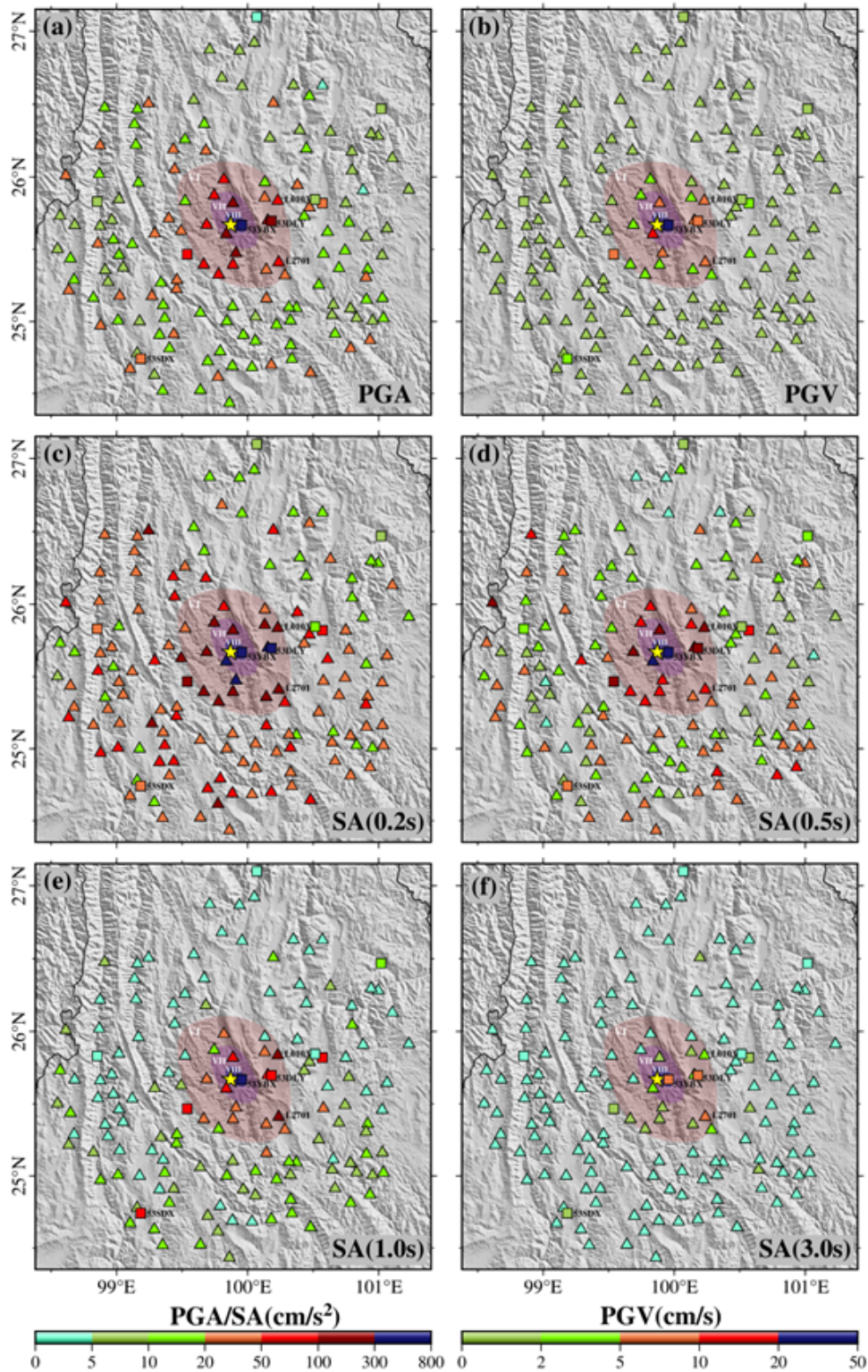


Figure 5

Comparison of horizontal (a) acceleration and (b) velocity time series, (c) response spectra for 5% damping ratio and (d) HVSR curves (H/V) of record 53BCJ on rock site with 53BTH on soil site.

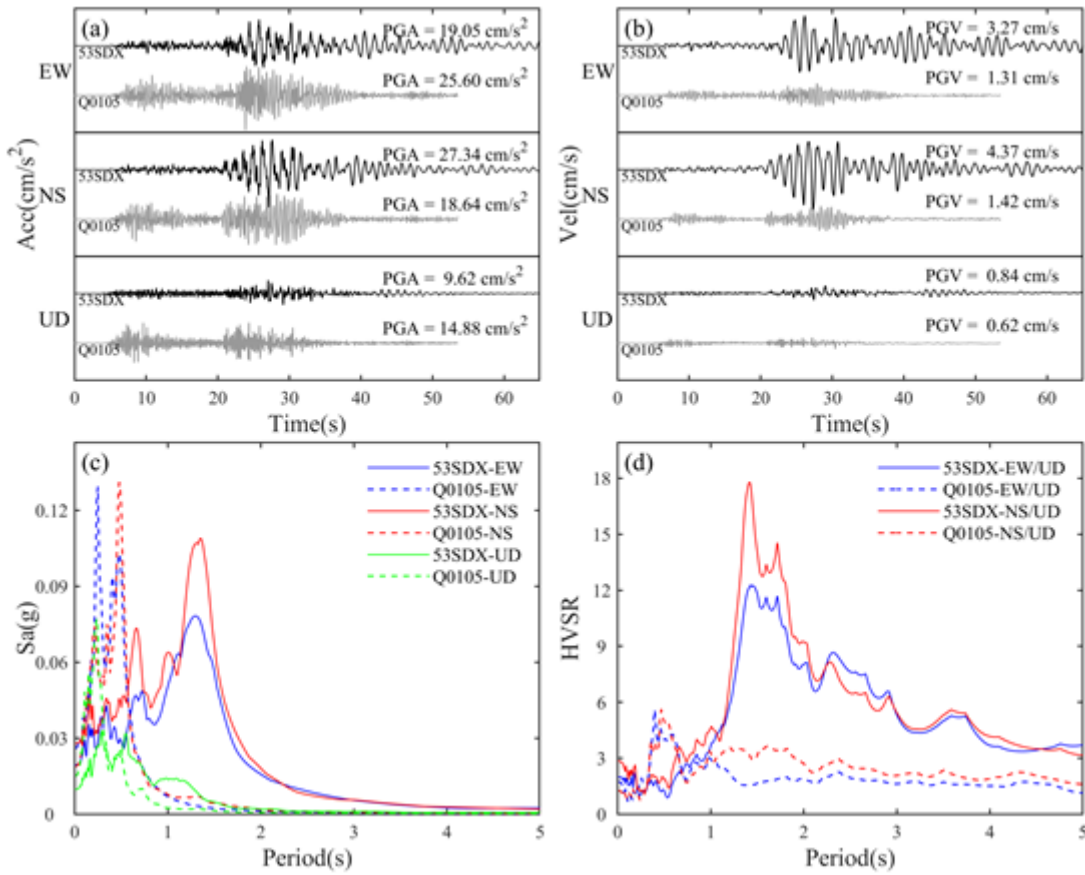


Figure 6

Three-component (a) acceleration and (b) velocity time series, (c) response spectra for 5% damping ratio, and (d) HVSR curves (H/V) of typical record Q0105 and 53SDX affected by local topography and soft sediments, respectively

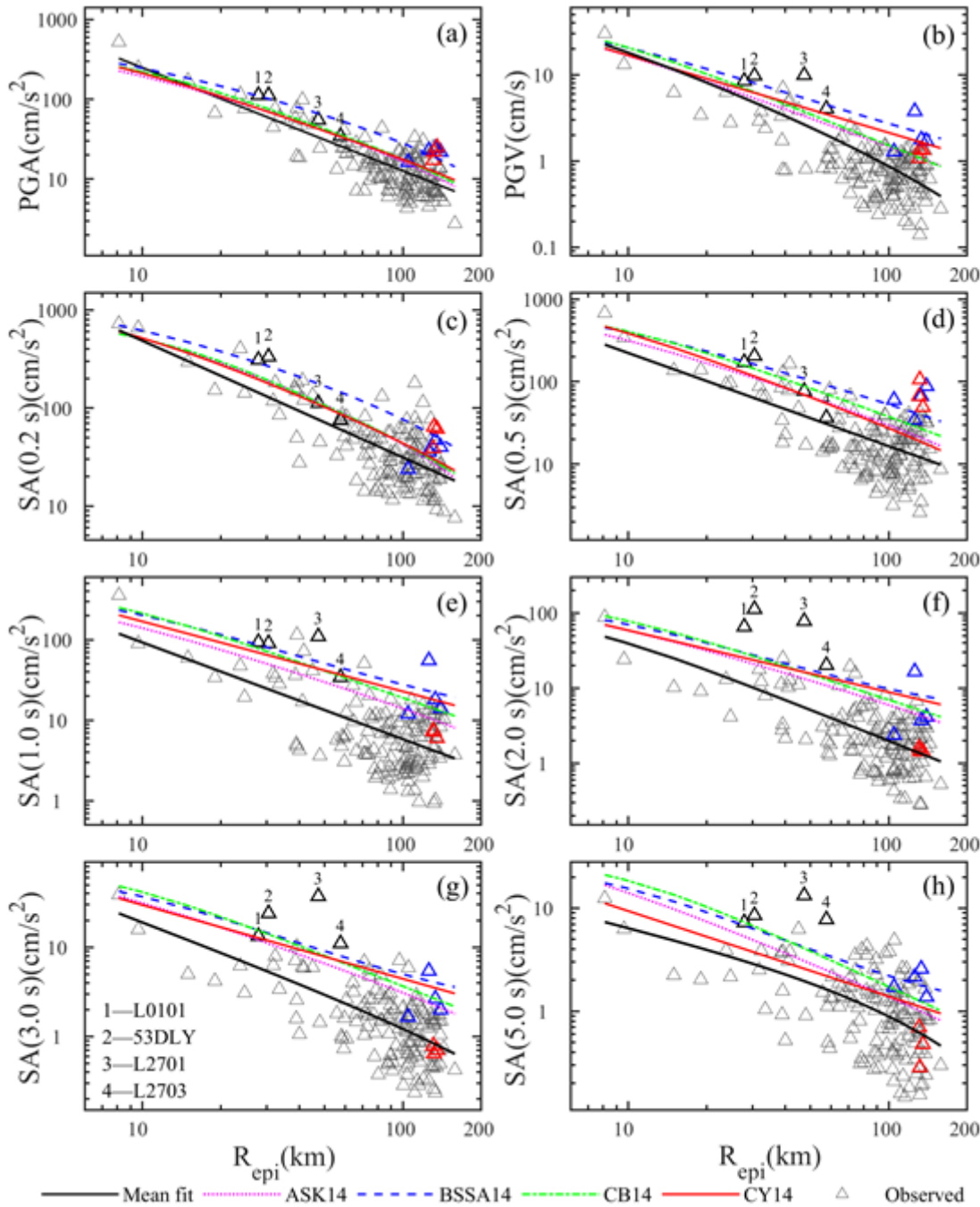


Figure 7

Variation of horizontal PGA, PGV and spectral acceleration values (5% damping) with distance. The blue and red triangles denote the observations strongly affected by local site effects due to soft sediments and topography respectively. ASK14, BSSA14, CB14 and CY14 denote median predictions from Abrahamson et al. (2014), Boore et al. (2014), Campbell and Bozorgnia (2014) and Chiou and Youngs (2014) model, respectively. The shear wave velocity are given representative values $V_{s30}=360\text{m/s}$.

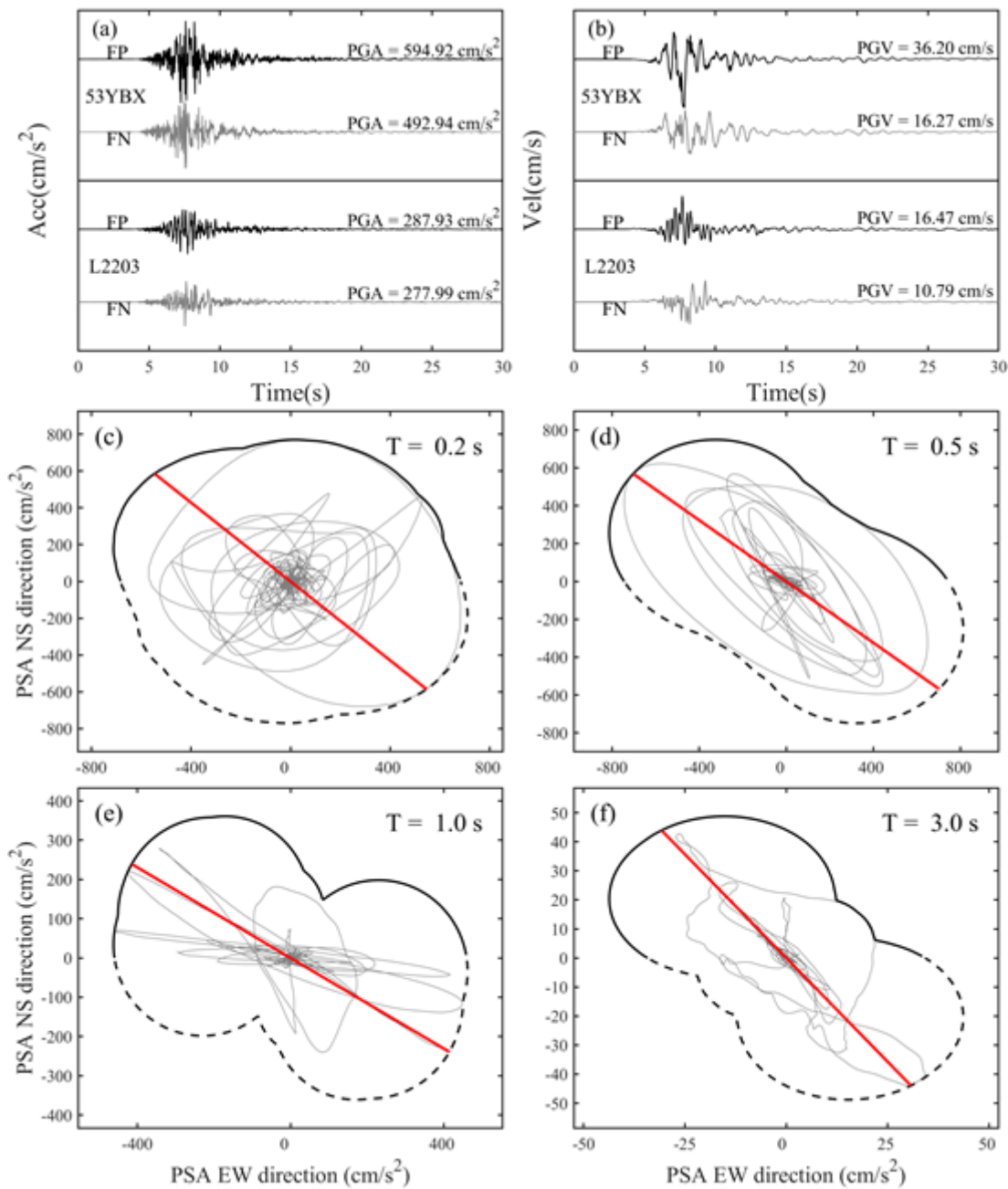


Figure 8

Fault parallel and fault normal component (a) acceleration and (b) velocity time series of the 53YBX and L2203 record, and directionality of a typical near-fault ground motion at 51YBX, shown as acceleration response trace for a 2-degree-of-freedom oscillator with $T =$ (c) 0.2 s, (d) 0.5 s, (e) 1.0 s, (f) 3.0 s.

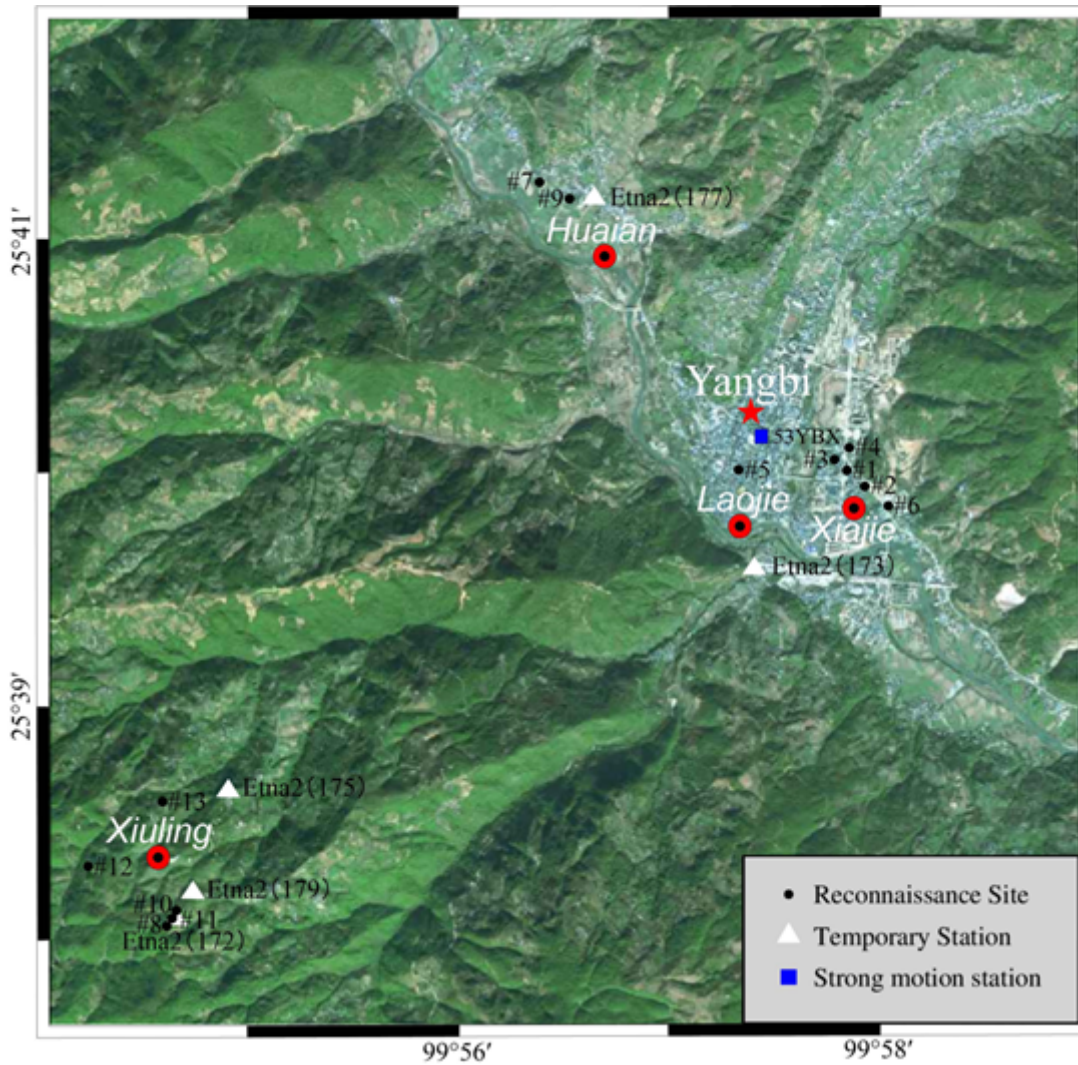


Figure 9

Location of seismic damage investigation sites and topographic array of strong motion observation in the most severely damaged Yangbi county close to the causative fault.



Figure 10

Earthquake damage differences along the FP and FN direction observed in Yangbi county town due to near-fault strong motion directionality. Comparison of two teaching buildings (RCF structure) along the (a) FN and (b) FP direction respectively in the primary school of Xiajie village in Yangbi county town (site #1), close to the 53YBX station; (c) comparison of two earth-wooden house in Huaian village north of Yangbi county town (site # 9), about 3km to the 53YBX station.

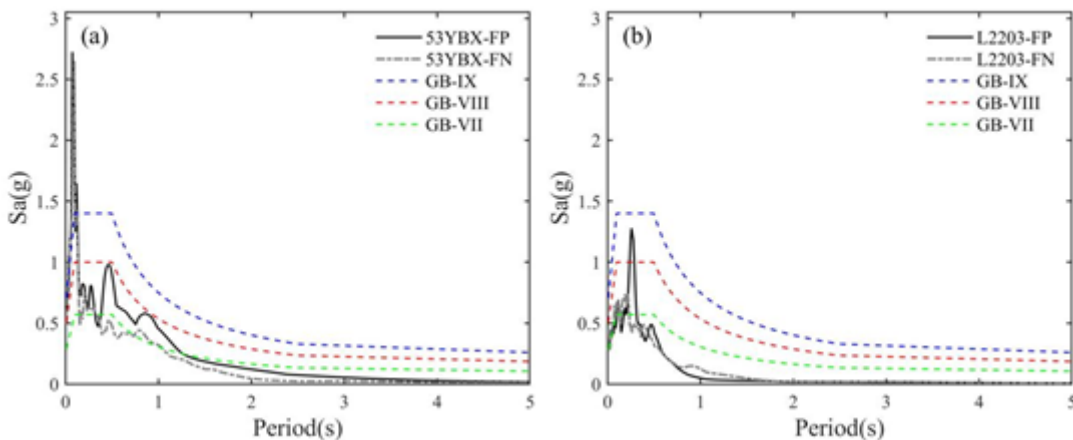


Figure 11

Fault parallel and fault normal component response spectra for 5% damping ratio of the (a) 53YBX and (b) L2203 record and comparison with code design spectra in China (MHURC, 2010).



Figure 12

Examples of structural damage observed in Yangbi county town during the reconnaissance mission. (a) earth wall collapse of a earth-wooden house in Xiajie village (site #2); (b) shear failure of earth-rockfill wall of a mosque in Xiajie village (site #3); (c-e) overall offset and collision of brick concrete buildings (site #4); (f) collapse of old earth-wooden houses in Laojie (site #5); (g) failure of old wooden columns due to decline in bearing capacity (site #6); (h) shear failure of courtyard wall in Huaian village (site #7); (i) collapse of gables in earth-wooden structures (site #8).



Figure 13

Examples of structural damage observed in Xiuling village close to the epicenter. (a) total collapse of adobe wall of an earth-wooden house (site #10); (b) wall collapse and roof falling of an earth-wooden house (site #11); (c) collapse of aged wooden frame roof of a brick concrete building (site #12); (d) damage differences along the FP and FN direction in two earth-wooden houses (site #13).